

# Nonhomogeneous Morphology and the Elastic Modulus of Aligned Carbon Nanotube Films

*Yoonjin Won<sup>a,l</sup>, Yuan Gao<sup>a</sup>, Roberto Guzman de Villoria<sup>b\*</sup>, Brian L. Wardle<sup>b</sup>,*

*Rong Xiang<sup>c+</sup>, Shigeo Maruyama<sup>c</sup>, Thomas W. Kenny<sup>a</sup>, Kenneth E. Goodson<sup>a</sup>*

<sup>a</sup> Department of Mechanical Engineering, 440 Escondido Mall, Stanford University, Stanford, CA 94305, USA.

<sup>b</sup> Department of Aeronautics and Astronautics, Massachusetts Institute of Technology, Cambridge, MA 02139, USA.

<sup>c</sup> Department of Mechanical Engineering, The University of Tokyo, Tokyo 113-8656, Japan.

<sup>\*</sup> Madrid Institutes for Advanced Research, Madrid, Spain (Current).

<sup>+</sup> School of Physics and Engineering, Sun Yat-sen University, Guangzhou 510275, China (Current).

KEYWORDS: Carbon nanotubes, CNT forest, modulus, stiffness, morphology, interfaces.

## **ABSTRACT**

Carbon nanotubes (CNT) arrays are interesting because of the combination of their small size and outstanding physical properties. Vertically aligned carbon nanotubes (VACNTs), also named CNT forests or CNT turfs, show high heat conductivity and sufficient mechanical compliance to accommodate thermal expansion mismatch for use as advanced thermal interface materials. This paper reports measurements of the in-plane moduli of single-walled CNT (SWCNT) and multi-walled CNT (MWCNT) films. The mechanical response of these films is related to the nonhomogeneous morphology of the grown nanotubes, such as entangled nanotubes of a top crust layer where growth begins. Aligned nanotubes in the middle region, and lower density nanotubes in the bottom layer where growth terminates. To investigate how the entanglement layer governs the mechanical moduli of CNT films, we eliminate the effect of the crust layer by etching the CNT films from the top. A microfabricated cantilever technique shows that crust removal reduces the resulting moduli of the etched SWCNT films by as much as 40%, whereas the moduli of the etched MWCNT films does not change significantly, suggesting a minimal crust effect on the film modulus for thick films ( $>90\ \mu\text{m}$ ). This improved understanding will allow us to engineer the mechanical properties of CNT films for future applications.

## **INTRODUCTION**

In electronic components, it is crucial to minimize the thermal resistances between the heat sink and heat spreader by minimizing air gaps. The surface roughness of planar surfaces limits the actual contact area between the two solids to values as low as 2% for lightly loaded interfaces<sup>1</sup>. These components also experience repeated temperature cycles that cause stresses at the

interface between the two different materials. Therefore, mechanically compliant thermal interface materials (TIMs) are used to join surfaces to improve heat transfer across the interface and minimize the effects of thermomechanical mismatch. Here, vertically aligned carbon nanotube (VACNT) films have been proposed as ideal TIMs due to their ability to combine the mechanical compliance of a polymer with the high thermal conductivity of a metal <sup>2-7</sup>.

While the out-of-plane elastic modulus has been studied using nanoindentation <sup>1,8</sup>, there is limited data available for the in-plane elastic modulus, *i.e.*, perpendicular to the primary direction of the CNTs. Past nanoindentation experiments have produced estimates of the out-of-plane (CNT axis direction) modulus ranging from 1 to 300 MPa as a result of film morphology variations <sup>2-11</sup>. Our past results using nanoindentation measurements show that out-of-plane modulus of MWCNT films ranging from 0.2 to 2.8 MPa <sup>8</sup>. These results suggest that the overall density, roughness, array height, and other physical characteristics may strongly influence the mechanical properties of VACNT films. Previous measurements of the in-plane modulus of VACNT films also suggested that the wide distribution of values of the modulus results from the variation of nanostructural features <sup>12-14</sup>. The nonhomogeneous characteristics of VACNT films have been confirmed by several studies using various types of measurements, such as scanning electron microscope (SEM), resonant Raman spectroscopy, and angle-resolved X-ray absorption <sup>15</sup>. Therefore, it is critical to relate the mechanical properties of VACNT films to variations (effectively this is spatial heterogeneity) in the morphology of the nanotube films. Performance of TIM materials as well as other VACNT-comprised structures <sup>16,17</sup>, particularly those used in microfabrication, will be directly affected by such structure-property heterogeneity, *e.g.*,

bioparticle separation elements and 3D structures formed via capillary infiltration of fluids into patterned arrays are likely very sensitive to such spatial heterogeneities<sup>18-20</sup>.

In this paper, a resonator technique is used to infer the in-plane modulus of vertically aligned SWCNT and MWCNT films using a laser Doppler vibrometer (LDV) to ascertain resonance shifts. We additionally investigate the modulus after removing the crust from the VACNT films using plasma etching to understand those local morphological effects on the overall mechanical responses.

## **RESULTS AND DISCUSSION**

We previously reported that nanotube characteristics such as alignment, density, and height impact the film's mechanical properties, including elastic modulus<sup>12</sup>. The nonhomogeneous regions of VACNT films exist because of their growth process which results in a denser and entangled crust layer above layers which can decrease in alignment towards the substrate<sup>21</sup>. Bedewy *et al.*<sup>15,22</sup> identified variations in morphology by investigating the growth height and density over time and correlating observed morphology changes to the growth process dynamics including catalyst diffusion and coarsening, and CNT population dynamics such as crowding, self-organization, and termination. These studies have revealed four different stages of the growth process. The first stage is the interweaving of a thin layer of entangled and randomly oriented nanotubes, which forms a crust on the top of the VACNT film. The crust extent varies for a given process depending on growth conditions. The crust is observed to be 1  $\mu\text{m}$  thick for the SWCNTs and 0.4  $\mu\text{m}$  thick for the MWCNTs in this work. The first stage begins the self-

organization that is manifested in the second stage morphology. The second stage is the vertically aligned growth beneath the top crust. In the third stage, the density decay stage, CNTs grow at the same speed as the previous stage, but the mass density per unit area can slowly decrease. This results in less aligned and less dense morphology in the bottom region of the film. The final stage is the termination step of the nanotube growth. An entire nanotube film is shown in Fig. 4b. Note that the third and fourth stages are dependent on the film height, i.e., if film height is controlled by quenching the growth process (removing carbon feedstock and/or temperature) to achieve a desired height that is less than the termination height allowed by catalyst evolution (typically in the range of 1 mm for MWCNT arrays), then stages 3 and 4 are less important. Detailed micrographs of a crust with a larger magnification are shown in Fig. 1a and b. The mechanical moduli of  $\sim 10 \mu\text{m}$ -thick SWCNT films and  $\sim 100 \mu\text{m}$ -thick MWCNT films are shown in Fig 2a and b. The SWCNT films have an in-plane modulus ranging from 40 to 80 MPa. The MWCNT films have low modulus around 1 MPa. There is no thickness dependency since the crust ( $0.5 - 1 \mu\text{m}$ -thick in this work) is  $< 0.5\%$  of the total thickness.

Past work shows a clear trend of decreasing in-plane modulus with increases in film thickness ranging from  $0.5\text{-}200 \mu\text{m}$  <sup>12,13</sup>. This is attributed to the presence of a thin and entangled crust layer as described above. The crust layer is more dense and probably stiffer than the middle layer. For use as an advanced TIM, CNT films usually are metallized, which then allows a metal layer to form a solder bond between a CNT film and target substrates <sup>23</sup>. The metallization is only about 200 nm thick. The solder penetrates the crust layer of the CNT film, which might decrease the crust effect on the mechanical properties of these films when used as TIMs. To understand the role of the crust layer, and to characterize films without the crust layer, we

developed an etch technique capable of removing the crust layer. The modulus measurements are carried out before and after the surface etching of the VACNT films to isolate and distinguish the effect of the crust on the properties of the film.

An O<sub>2</sub> plasma etch process is used to remove the crust and top layer of the VACNT films resulting in a reduction of the VACNT film thicknesses<sup>24</sup>. We have used RF power (45 W) or O<sub>2</sub> flow rate (80 sccm), resulting in the etching rate as 1-2 μm/min. Figure 1 shows SEM micrographs of MWCNTs before and after O<sub>2</sub> plasma etching. In Fig. 1a and b, the tips of CNTs are entangled, forming a wavy crust layer. Figure 1c shows that the top crust layer of CNTs is removed by the O<sub>2</sub> plasma etching. The transformed morphology is clearly illustrated in a close-up view in Fig. 1d. Some tips of CNTs attach and fix themselves to each other, forming needle shapes instead of displaying entanglements. In Fig. 1c and d, CNTs appear more vertically oriented after the etching than they were before the etching. This enhancement in vertical orientation may be associated with the effect of a strong vertical electric field during the plasma etch process, which may induce vertical alignment of the CNTs<sup>25</sup>.

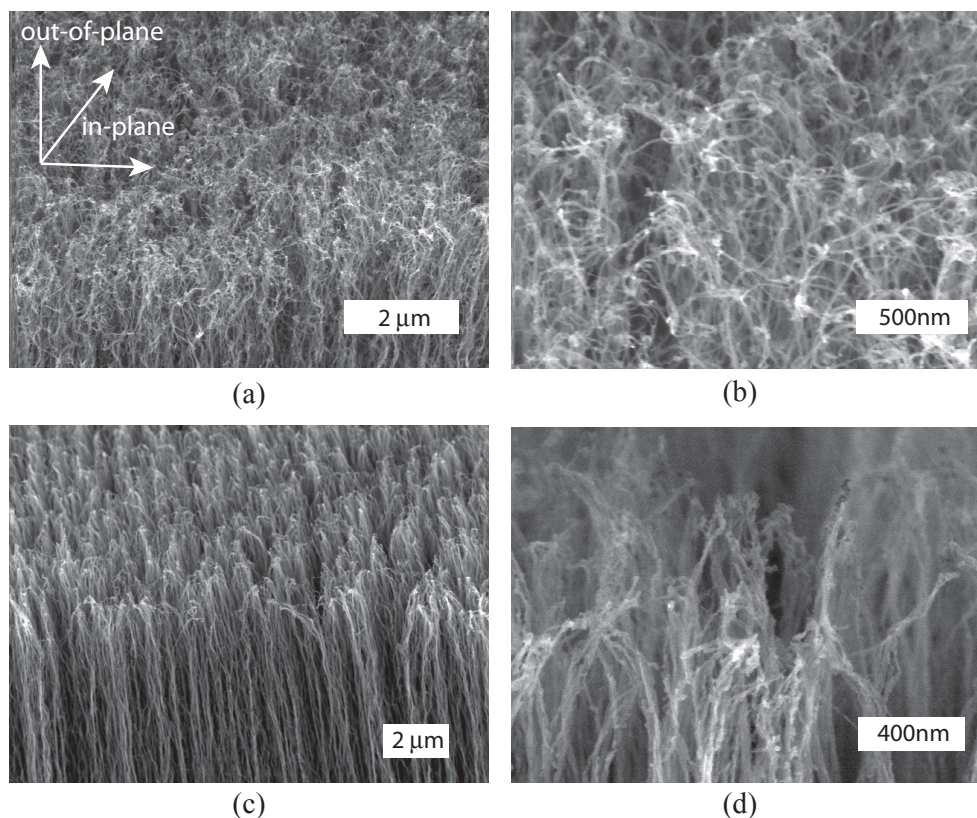


**Figure. 1.** SEM images of MWCNT films before and after the surface etching. (a) SEM image of a crust layer. (b) Close-up view of the crust. SEM images show many entanglements within the crust layer. (c) CNTs after the surface etching (d) Close-up view of CNTs after the surface etching. These SEM images indicate that morphology is changed after the surface etching.

The SWCNT films received a 1-minute surface etch. This etch reduces the film thickness from 11-14  $\mu\text{m}$  to 9-12  $\mu\text{m}$  and removes the crust layer. Since the portion of the crust is relatively large (7%-11% of the film thickness), the crust can significantly affect the mechanical properties of the film. In Fig. 2a, the moduli before the etching are shown with black squares, and the moduli after the etching are represented with gray crosses. The crust layer on these films is about  $\sim 1 \mu\text{m}$ . Figure 3 shows that the modulus of as-grown films increases as the film thickness decreases due to the impact of the crust on the modulus. Figure 2a shows that the etched films

have lower modulus after the plasma etch. This reduction of modulus for thinned films is the opposite of the previous trend for the dependence of modulus on film thickness because of the removal of the crust layer in this experiment. The remaining film comprises of the middle and base layers, which have a lower in-plane modulus than the crust. Therefore, the moduli of the entire films without the top crust layer will be decreased; the moduli of the etched films are smaller than the grown films with same heights.

The MWCNT films have lower density, alignment, and more significant density decay in the bottom layer than the SWCNT films. These MWCNT films received a 5-minute surface etch. This etching removes the top crust and reduces the film thickness from 95-115  $\mu\text{m}$  to 90-105  $\mu\text{m}$ . In Fig. 2b, the moduli before and after etching of the MWCNT films are represented with blue squares and crosses, respectively. There is no significant difference in modulus between the etched and as-grown films. For thick films ( $>90 \mu\text{m}$ ), the crust of ( $\sim 0.4 \mu\text{m}$ ) occupies a smaller portion of the entire film ( $<0.5\%$ ); the crust effect on the extracted modulus is low.

In addition to the crust effect, the low modulus of MWCNT films may be attributed to the bottom region of the thick films resulting from the density decay stage<sup>15,22</sup>. This bottom region of sparse or unaligned nanotubes might reduce the mechanical modulus of an entire film.

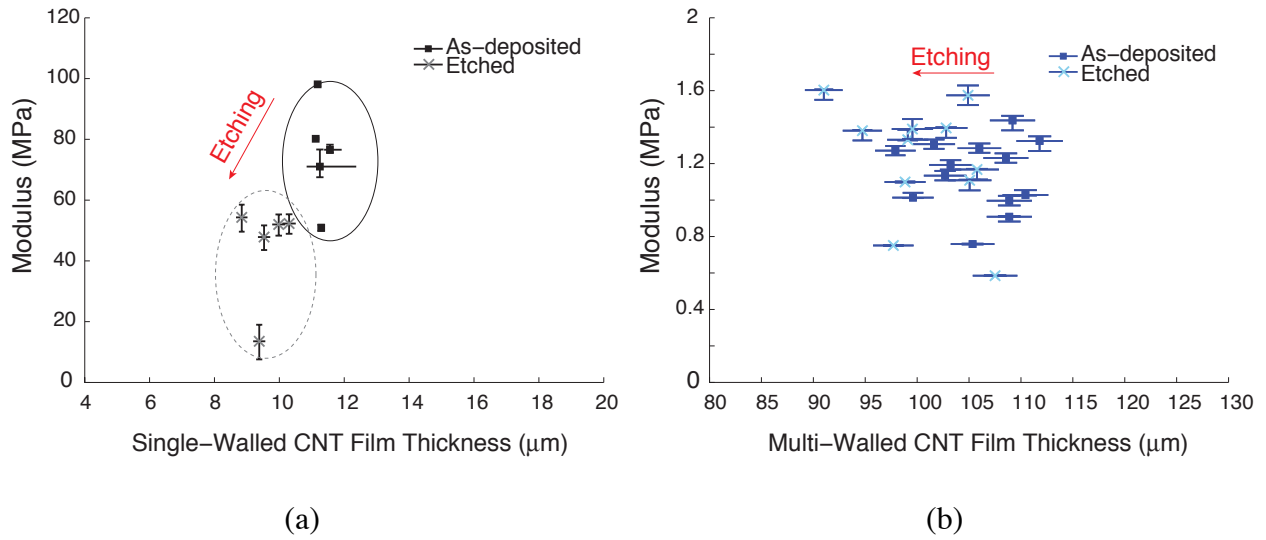


**Figure. 2.** Effective modulus of (a) SWCNT films and (b) MWCNT films after the surface etch. Solid squares and crosses represent the moduli before and after the etching, respectively (will be polished). The thickness nonuniformities are indicated by the horizontal error bars. Their effects on the modulus are represented by the vertical error bars. Although the thick (MWCNT) films exhibit relatively large thickness nonuniformities, the effects on the modulus are reasonably small.

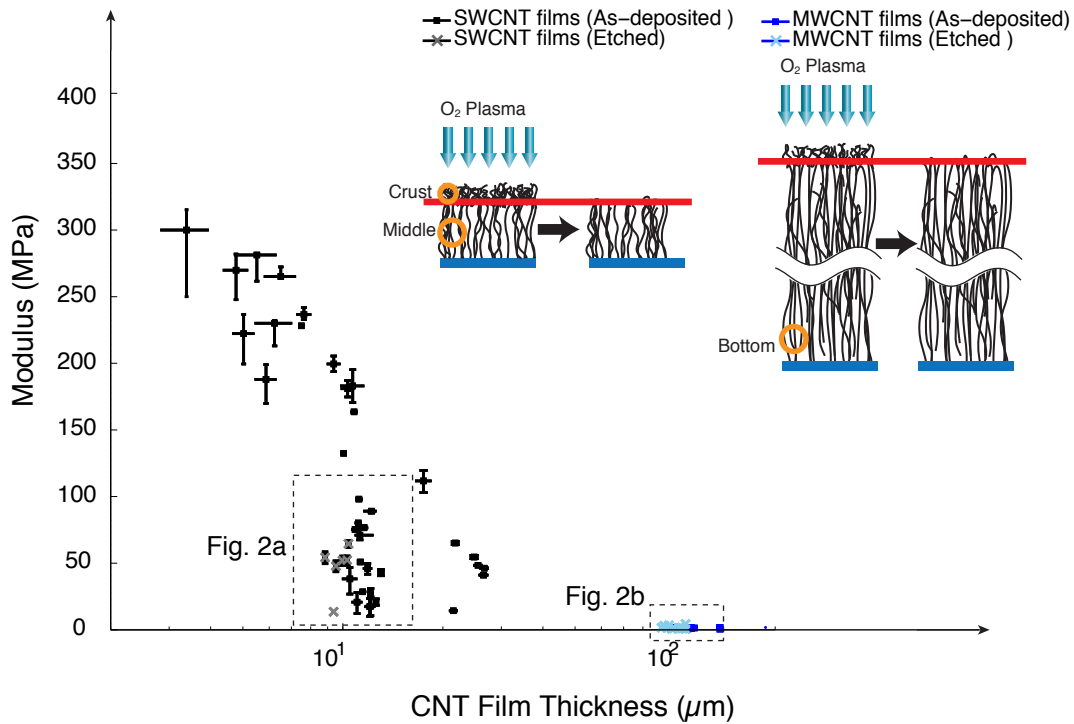


**Figure. 3.** Modulus of SWCNT and MWCNT films before and after the surface etching. Data sets show that the modulus decreases as film thickness increases. Schematics of vertically aligned CNT films of SWCNT and MWCNT films before and after the etching. SWCNT film has the crust and middle layer, and MWCNT (>90 μm) film has the crust, middle, and bottom layer.

## CONCLUDING REMARKS

In this paper, a microfabricated resonator technique is used to measure the in-plane moduli of ~10 μm-thick vertically aligned SWCNT films and ~100 μm-thick vertically aligned MWCNT films to be in the range of 80 MPa and 1 MPa, respectively. The mechanical data sets show the strong dependence of the SWCNT film modulus on film thickness due to morphology variations

(crust, middle, and bottom regions) through the film thickness, with no observed effect for the MWCNT films in the thickness ranges considered ( $\sim 100 \mu\text{m}$  thick films). Removal of the unaligned crust layer reduces the in-plane modulus, consistent with micromechanics of aligned and unaligned fibrous structures. To use these VACNTs as TIMs, the crust region and bottom region of the VACNT film will be embedded in thin metal layers for use in a solder bonding process. Therefore, it is particularly important to isolate and understand the effect of the crust on the metal deposition and the resulting mechanical properties of CNT films. The surface etching removes the crust of entangled nanotubes from the VACNT film and changes the film thickness, as revealed in SEM images. The moduli of the films before and after etching measured in this work and in past work, and the images of SWCNT and MWCNT films before and after the etching are shown in Fig. 3. Because of the large effect of the crust on the measured modulus values, the etching increases the mechanical compliance of the SWCNT films ( $\sim 10 \mu\text{m}$ ), which is suitable for use as an interface material. Regardless of the presence of the crust, the range of the low mechanical moduli of MWCNT films is promising for a variety of applications including thermal interfaces. Future work will address potential changes in morphology associated with surface etching. The new morphology may induce differences in nonuniformity and density, which can affect the mechanical behaviors of the entire films. To account for those factors, the etched films should be characterized using other techniques, such as Raman spectroscopy or X-ray absorption in the future. Our plans for future work also include studies of bonding materials and integration of the CNT TIM between two surfaces that have different coefficients of thermal expansion.

## METHODS

### Materials

The fabrication of the Si cantilevers includes two deep reactive-ion etching (DRIE) processes in serial order to define cantilever outlines and substrates open at the bottom. This is followed by removal of the oxide layer, which is used as an etch stop layer for the DRIE process. The processed wafer is cleaved into several pieces, which receive differing thicknesses of CNT films through exposure to different numbers of growth intervals. The fabrication process of the microcantilevers and standard etching procedures are detailed elsewhere<sup>12</sup>.

Vertically aligned SWCNT films are grown on fabricated cantilevers using an alcohol catalytic chemical vapor deposition process at the Maruyama lab at the University of Tokyo, and detailed in references<sup>26</sup>. Before the growth, a 50 nm SiO<sub>2</sub> layer is first grown on the substrates and the catalyst films (10 nm-thick Al and 0.2 nm-thick Co) are deposited. SWCNT films are then synthesized using ethanol (1.3 kPa) as the carbon source at 800°C for different time frames. During the synthesis, CNT film thicknesses are controlled by optical absorbance, using the relative transmitted intensity of the incident laser. Additional analysis of SWCNTs reveals that the growth provides almost 100% SWCNTs with the number density of 10<sup>12</sup> cm<sup>-2</sup><sup>27,28</sup>.

Vertically aligned MWCNT films are grown using a chemical vapor deposition process at the Wardle lab at MIT, as described in references<sup>29-31</sup>. Prior to CVD, Al<sub>2</sub>O<sub>3</sub>/Fe layers are deposited, and all pre-heater gas lines (He, H<sub>2</sub>, and C<sub>2</sub>H<sub>4</sub>) are flushed for 10 minutes followed by 10

additional minutes of He to displace trapped air from the system. To condition the catalyst film and produce metallic nanoparticles, the furnace is quickly brought to 750°C. A flow of He (73 sccm) and H<sub>2</sub> (400 sccm) is then introduced over the target substrate for 5 minutes. A mixture of He/H<sub>2</sub>/C<sub>2</sub>H<sub>4</sub> (73/400/200 sccm) is introduced for reference substrates during which the CNT array emerges. Finally, the system is cooled to ambient while flushing He to eliminate any reactive gases from the system. The resulting thickness of MWCNT films provides a relatively thick film with CNT number density of  $\sim 10^{10} \text{ cm}^{-2}$ .

### Data Interpretation of In-Plane Modulus

Scanning electron microscope (SEM) images reveal that the actual arrangements are substantially complicated, showing many crossings and connections between CNTs as shown in Fig. 1. We assume that a VACNT film behaves as a solid and continuous material structure where all the tube crossings are linked. Based on this continuum assumption, a resonator measurement technique is used to extract the effective in-plane moduli of CNT films.

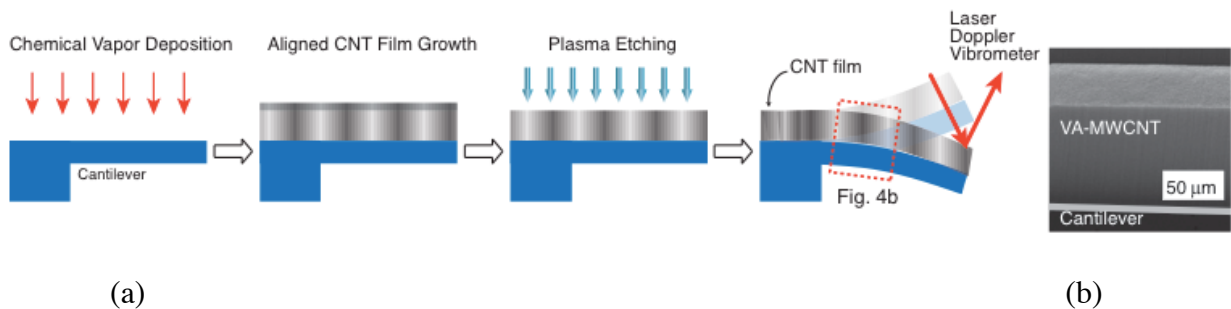


**Figure 4.** (a) Schematic of the mechanical characterization process of in-plane modulus using a Si-CNT composite beam before and after the etch. Beam dimensions are scaled to achieve a

range of resonant frequencies. VACNT film thicknesses are also varied to characterize the mechanical properties of different layer thicknesses (b) SEM image of a Si-MWCNT composite beam.

The resonator technique infers the mechanical properties of the tested film, such as effective in-plane modulus. A laser Doppler vibrometer (LDV) characterizes the mechanical properties of the nanostructured film by capturing the resonant frequency of the cantilevers before and after the film growth. The cantilevers are mounted on a piezoelectric shaker inside a vacuum chamber with optical access for the LDV procedure. The shaker is driven by a 150 mV white noise input with frequency ranging from 1 kHz to 350 kHz and amplified at fixed gain of 100 X by a Krohn-Hite 7500 Widebands Power Amplifier. The beam from the LDV (Polytec OFV 2500) hits the end of the cantilever. The Doppler shift  $f_D (= 2 \cdot v_{\text{beam}}/\lambda_{\text{laser}})$  is then captured to calculate the velocity component of the object, where  $\lambda_{\text{laser}}$  is the laser wavelength. The velocity output is converted to voltage signal with a factor of 10 mm/sV, and is connected to a vector signal analyzer (HP89441A). The frequency spectra on the vector signal analyzer indicates peaks of the modes of vibration, and they are recorded in a PC via GPIB (NI-GPIB-USB-HS, National Instruments). The GPIB controls the operating power and the frequency range of the shaker.

For the resonant frequency calculation of a composite beam, we use the effective  $\overline{EI}$  and  $\overline{\rho A}$  where  $E$ ,  $I$ ,  $\rho$ , and  $A$ , are respectively the modulus, the second moment of area, density, and cross-sectional area of the beam. Here, the  $\overline{EI}$  and  $\overline{\rho A}$  for a beam with multi-layers are  $\overline{EI} = \sum_i E_i I_i$  and  $\overline{\rho A} = \sum_i \rho_i A_i$ <sup>32</sup>. Therefore, the effective modulus of CNT film can be extracted as<sup>12</sup>

$$E_{CNT} = \frac{E_{Si}}{I_{CNT}} \left( \left( 1 + \frac{\rho_{CNT} A_{CNT}}{\rho_{Si} A_{Si}} \right) \cdot (1 + \Delta)^2 I_{Si_0} - I_{Si} \right) \quad (1)$$

The subscripts,  $Si_0$ ,  $Si$ , and  $CNT$  denote the silicon layer of a silicon-only cantilever, the silicon, and VACNT layer of a Si-CNT composite cantilever, respectively, and  $\Delta$  is the ratio of the resonant frequency shift with the Si-CNT beam to the original resonant frequency of the silicon beam. Then, we use the transformed section method that converts the cross-section of a composite beam into an equivalent cross-section of an imaginary beam, which is then modeled as one material<sup>31</sup>. The distance  $y$  to the centroid, values of  $I_{Si_0}$ ,  $I_{Si}$ ,  $I_{CNT}$ <sup>12,32,33</sup> and  $\Delta$  from the measurement are used as input parameters to Eq. (1). Here,  $E_{CNT}$  is a function of  $I_{CNT}$ , while  $E_{CNT}$  impacts  $y$  and  $y$  impacts  $I_{CNT}$ . Because of this modulus weighted centroid calculation, we do iteration to find the correct  $E_{CNT}$  and  $I_{CNT}$  using Matlab code. The density ( $\rho_{CNT}$ ), another input parameter to Eq. (1), is estimated based on thickness and mass measurement of CNT layer using a microbalance (SE2 Ultra Micro Balance, Sartorius) and cross-sectional SEM.

We validate this methodology with a finite element method (FEM) model, by using a film with same modulus and thickness to compare the resonant frequency shift<sup>13</sup>. A good agreement between the measurements and simulation has been observed for thin films. However, modulus

is particularly underestimated for thick films, which introduces a modification factor. This might be because of transverse shear strain or damping effect, which are usually more significant for thick films.

## ACKNOWLEDGMENT

This work was sponsored by the Office of Naval Research, SRC, the MARCO IFC, the Air Force Office of Scientific Research (AFOSR) through FA9550-12-1-0195, and the National Science Foundation. At the University of Tokyo, this work was supported by Grant-in-Aid for Scientific Research (22226006 and 25630063), Indium replacement by single-walled carbon nanotube thin films (IRENA) Project by Japan Science and Technology Agency and Strategic International Collaborative Research Program. At MIT, this work was supported by Boeing, EADS, Embraer, Lockheed Martin, Saab AB, Composite Systems Technology, Hexcel, and TohoTenax through MIT's Nano-Engineered Composite aerospace Structures (NECST) Consortium. We performed this work in part at the Stanford Nanofabrication Facility (a member of the National Nanotechnology Infrastructure Network), which is supported by the National Science Foundation under Grant ECS-Integrated Systems. At MIT, this work was carried out in part through the use of MIT's Microsystems Technology Laboratories and made use of the MIT MRSEC Shared Experimental Facilities supported by the National Science Foundation under award number DMR-0819762.

## REFERENCES

- (1) Prasher, R. *Proceedings of the IEEE* **2006**, *94*, 1571–1586.
- (2) Xu, J.; Fisher, T. S. *Components and Packaging Technologies* **2006**, *29*, 261–267.
- (3) Cola, B. A.; Xu, X.; Fisher, T. S. *Applied Physics Letters* **2007**, *90*, 093513.
- (4) Cola, B. A.; Xu, J.; Fisher, T. S. *International Journal of Heat and Mass Transfer* **2009**, *52*, 3490–3503.
- (5) Panzer, M.; Zhang, G.; Mann, D.; Hu, X.; Pop, E.; Dai, H.; Goodson, K. *Journal of Heat Transfer* **2008**, *130*, 052401.
- (6) Marconnet, A. M.; Panzer, M. A.; Goodson, K. E. *Reviews of Modern Physics* **2013**, *85*, 1295–1326.
- (7) Marconnet, A. M.; Yamamoto, N.; Panzer, M. A.; Wardle, B. L.; Goodson, K. E. *ACS nano* **2011**, *5*, 4818–4825.
- (8) Gao, Y.; Kodama, T.; Won, Y.; Dogbe, S.; Pan, L.; Goodson, K. E. *Carbon* **2012**, *50*, 3789–3798.
- (9) Tong, T.; Zhao, Y.; Delzeit, L.; Kashani, A.; Meyyappan, M.; Majumdar, A. *IEEE*

- Trans. Comp. Packag. Technol.* **30**, 92–100.
- (10) Maschmann, M. R.; Zhang, Q.; Du, F.; Dai, L.; Baur, J. *Carbon* **2011**, *49*, 386–397.
  - (11) Mesarovic, S.; McCarter, C.; Bahr, D.; Radhakrishnan, H.; Richards, R.; Richards, C.; McClain, D.; Jiao, J. *Scripta Materialia* **2007**, *56*, 157–160.
  - (12) Won, Y.; Gao, Y.; Panzer, M. A.; Dogbe, S.; Pan, L.; Kenny, T. W.; Goodson, K. E. *Carbon* **2012**, *50*, 347–355.
  - (13) Won, Y.; Gao, Y.; de Villoria, R. G.; Wardle, B. L.; Kenny, T. W.; Goodson, K. E. *Proceedings of the Thirteenth InterSociety Conference on Thermal and Thermomechanical Phenomena in Electronic Systems* **2012**, 1070–1076.
  - (14) Won, Y.; Wang, E. N.; Goodson, K. E.; Kenny, T. W. *International Journal of Thermal Sciences* **2011**, *50*, 325–331.
  - (15) Bedewy, M.; Meshot, E. R.; Reinker, M. J.; Hart, A. J. *ACS nano* **2011**, *5*, 8974–8989.
  - (16) Vaddiraju, S.; Cebeci, H.; Gleason, K. K.; Wardle, B. L. *ACS Appl Mater Interfaces* **2009**, *1*, 2565–2572.
  - (17) Zhang, J.; Lu, H.; Sun, Y.; Ci, L.; Ajayan, P. M.; Lou, J. *ACS Appl Mater Interfaces* **2013**, *5*, 9501–9507.
  - (18) Noorduyn, W. L.; Grinthal, A.; Mahadevan, L.; Aizenberg, J. *Science* **2013**, *340*, 832–837.
  - (19) De Volder, M.; Tawfick, S. H.; Park, S. J.; Copic, D.; Zhao, Z.; Lu, W.; Hart, A. J. *Advanced Materials* **2010**, *22*, 4384–4389.
  - (20) Fachin, F.; Chen, G. D.; Toner, M.; Wardle, B. L. *Microelectromechanical Systems, Journal of* **20**, 1428–1438.
  - (21) Zhang, L.; Li, Z.; Tan, Y.; Lolli, G.; Sakulchaicharoen, N.; Requejo, F. G.; Mun, B. S.; Resasco, D. E. *Chemistry of materials* **2006**, *18*, 5624–5629.
  - (22) Bedewy, M.; Meshot, E.; Guo, H.; Verploegen, E.; Lu, W.; Hart, A. *The Journal of Physical Chemistry C* **2009**, *113*, 20576–20582.
  - (23) Barako, M. T.; Gao, Y.; Marconnet, A. M.; Asheghi, M.; Goodson, K. E. **2012**, 1225–1233.
  - (24) Liu, Y.; Liu, L.; Liu, P.; Sheng, L.; Fan, S. *Diamond and Related Materials* **2004**, *13*, 1609–1613.
  - (25) Huang, S.; Dai, L. *The Journal of Physical Chemistry B* **2002**, *106*, 3543–3545.
  - (26) Murakami, Y.; Chiashi, S.; Miyauchi, Y.; Hu, M.; Ogura, M.; Okubo, T.; Maruyama, S. *Chemical Physics Letters* **2004**, *385*, 298–303.
  - (27) Hu, M.; Murakami, Y.; Ogura, M.; Maruyama, S.; Okubo, T. *J Catal* **2004**, *225*, 230–239.
  - (28) Duong, H. M.; Einarsson, E.; Okawa, J.; Xiang, R.; Maruyama, S. *Japanese Journal of Applied Physics* **2008**, *47*, 1994–1999.
  - (29) Villoria, R.; Figueredo, S.; Hart, A.; III, S. A. S.; Slocum, A. H.; Wardle, B. L. *Nanotechnology* **2009**, *20*, 405611.
  - (30) García, E.; Hart, A.; Wardle, B. *AIAA journal* **2008**, *46*, 1405.
  - (31) Wardle, B. L.; Saito, D. S.; Garcia, E. J.; Hart, A. J.; de Villoria, R. G.; Verploegen, E. A. *Advanced Materials* **2008**, *20*, 2707–2714.
  - (32) Voiculescu, I.; Zaghloul, M.; McGill, R. *Proceedings of the Institution of Mechanical Engineers* **2006**, *220*, 1601–1608.
  - (33) Gere, J. *lavoisier.fr* **2003**.